Comparative Analysis of Vibration and Noise in IPMSM Considering the Effect of MTPA Control Algorithms for Electric Vehicles

Zexiu Han, *Member, IEEE*, and Jinglin Liu, *Member, IEEE*

***Abstract*—For many servosystems in electric vehicles (EVs), high-performance controls of permanent magnet synchronous motor (PMSM) drives are widely used due to their high efficiency and low vibration and noise. In order to ensure the high efficiency of the servosystems, some online and offline maximum torque per ampere (MTPA) control strategies are proposed; meanwhile, the vibration and noise of interior PMSMs (IPMSMs) in these servosystems for EVs must be smooth and soft. In this article, the vibration and noise of the IPMSM based on MTPA control algorithms are evaluated and compared. First, the influence of the voltage inverter on the noise of IPMSM is presented in detail and the relationship between the harmonic frequencies of the air gap magnetic force and the vibration frequencies of the IPMSM is investigated. Then, combined with this relationship, the effect principle of the control strategies on the magnetic vibration of the IPMSMs is defined. Based on this definition, the operation process and noise mechanism of different control methods are discussed. Finally, the performance of the vibration and noise under classical field-oriented control, offline MTPA control, and online MTPA control is concluded. With the comprehensive analysis and overview provided in this article, it is significant to guide the selection of a high-performance control method for servosystems in EVs.**

***Index Terms*—Interior permanent magnet synchronous motor (IPMSM), maximum torque per ampere (MTPA), noise, vibration.**

I. Introduction

AT PRESENT, interior permanent magnet synchronous motors (IPMSMs) have been widely used for electric vehicles (EVs). As an important component of EVs, high-performance IPMSM systems are in high demand [1]–[3]. For an EV, it has to be paid special attention to the temperature rise and noise when the high-performance IPMSM achieves basic operational functions. Fig. 1 shows the requirements of the high-performance motor. The IPMSM control system can not only operate accurately and efficiently [4]–[6], but also the motor should generate less heat and low noise [7] [8]. In general, one of the benefits of high efficiency is that it can reduce the temperature rise of the motor. Therefore, in order to improve the efficiency, many maximum torque per ampere (MTPA) control strategies based on the field-oriented control (FOC) method have been proposed and they do require less stator current, which reduces the temperature rise of the motor. Actually, the MTPA control methods also have positive effects on reducing motor vibration and noise. As a consequence, if different MTPA control strategies are used to improve the efficiency, the characteristics of the vibration and noise of the IPMSM are quite different [9].

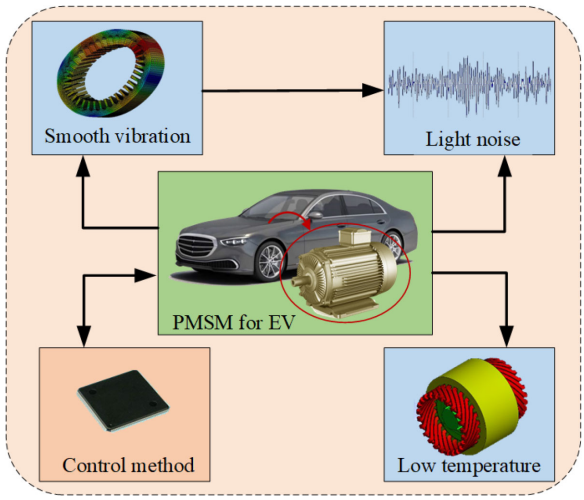

Fig. 1. High-performance IPMSM control system.

Under the same mechanical assembly conditions, the different control methods of the IPMSM mainly affect the electromagnetic vibration and noise. In addition, if the vibration and noise of the motor cannot be effectively suppressed, the control methods that can improve the efficiency still cannot be applied in high-performance applications for EVs. In many papers, researchers have proposed some effective MTPA control algorithms [10]–[12]. According to the control process, these control algorithms can be divided into offline methods and online methods. The most popular offline method is the MTPA control strategy based on the look-up table (LUT) method [13]. For this method, reasonable d- and q-axis current references are obtained from the LUT, which is generated in a series of preset experiments. As a feasible and effective online MTPA control

Manuscript received July 6, 2020; revised September 15, 2020; accepted October 23, 2020. Date of publication November 6, 2020; date of current version February 5, 2021. This work was supported in part by the National Natural Science Foundation of China under Grant 51907161 and in part by the Fundamental Research Funds for the Central Universities under Grant 3102019ZDHQD02. Recommended for publication by Associate Editor L. V. Iyer. *(Corresponding author: Jinglin Liu.)*

The authors are with the Shaanxi Key Laboratory of Small and Special Electrical Machine and Drive Technology, School of Automation, Northwestern Polytechnical University, Xi'an 710129, China (e-mail: hanzexiu1990@outlook.com; jinglinl@nwpu.edu.cn).

Color versions of one or more of the figures in this article are available online at https://ieeexplore.ieee.org.

Digital Object Identifier 10.1109/TPEL.2020.3036402

strategy, the virtual signal injection method is proposed to track the MTPA points in some new lectures [14], [15]. A small sinusoidal signal is added to the measured stator current angle mathematically and the torque derivative is obtained through various filters to generate the desired *d*-axis current. These papers fully demonstrate the effective control effect of offline and online MTPA control strategies on IPMSMs; however, under these control strategies, the vibration and noise characteristics of IPMSM are rarely detailed and comparatively analyzed.

In the past several years, many researchers have done extensive research on the analysis and optimization of vibration and noise in IPMSM [16]–[27]. Some effective research studies focused on explaining the influence of motor structure parameters on vibration and noise. In [16], different pole and slot combinations were the core structure parameter, and the influence of this parameter on vibration and noise was shown in detail. In [17], when the motor adopts different skewed slots, the characteristics of vibration and noise were analyzed. In [18], rotor slits on the rotor's outer circumference was adopted to reduce acoustic noise and vibration in an IPMSM. There are also important research studies trying to find methods to accurately predict vibration and noise. In [19], a numerical model to predict acoustic noise due to electromagnetic forces in IPMSM was presented. In [20], an analytical model was developed to predict electromagnetic forces, and then four different PMSM topologies are compared for their performances with regard to noise and vibration. In [21], a novel black and white box method was presented to diagnose the noise of the IPMSM. In [22], the force analysis was based on the field reconstruction method, which is a very efficient technique for predicting vibration and noise. In addition, a lot of meaningful research studies focus on the effects of current harmonics on noise and vibration. In [23], the strong influence of the current harmonics on the acoustic level of a synchronous machine is clearly shown. In [24], the effects of the current harmonics from inverter operation on the additional electromagnetic noise were analyzed. In [25], vibration and noise under different supply currents were investigated, and the variation patterns of the noise and vibration peaks were explained by the amplitude changes of the lowest spatial order force due to current harmonics. For an important goal, many research studies have been used to reduce noise and vibration in PMSM. In [26], the rotor shape especially geometry of flux barrier was optimized to meet reduction design of electromagnetic exciting forces that affect the noise and vibration. In [27], an optimal choice of the carrier frequency, by an optimization method, allowed for a reduction of the vibration in the targeted machine under different operating conditions.

In comparison, this article aims to explore the mechanism of vibration and noise in IPMSM based on space voltage vector control technology. Then, the relationship between the electromagnetic force and the control characteristics based on the vector control strategy is summarized, and the characteristics of the vibration and noise of the motor are obtained. At last, combined with the electromagnetic analysis, modal analysis, vibration analysis, and noise analysis, the correctness of the laws is verified by experiment. The goal of this article is to evaluate and compare the vibration and noise in IPMSM, which is controlled by MTPA strategies to achieve low copper loss and high-efficiency operation. Different from the previous research on the common mechanism of motor vibration and noise, this article combines the widely used MTPA control strategies to show the characteristics of vibration and noise in IPMSM. The research content can play an important guiding role in the application of electric power assist systems such as small EVs.

II. Mathematical Model of System

A. Conditions and Assumptions of Analysis

The noise of IPMSM can be divided into mechanical noise, electromagnetic noise, and aerodynamic noise. Among them, the mechanism of electromagnetic noise is complicated. More importantly, the sound quality of electromagnetic noise is poor, and it is often manifested as high-frequency whistling, which can make human feel very uncomfortable.

The electromagnetic noise of the motor is caused by electromagnetic force, wherein the electromagnetic force can be divided into Maxwell force and magnetostrictive force. In general, the noise caused by the magnetostrictive force is very small. Therefore, only the Maxwell force is discussed in this article.

According to the structure of the electrical machines, the electromagnetic force can be divided into the tangential force and the radial force. Generally, the effect of tangential electromagnetic force on motor noise is not significant. The radial electromagnetic force in the direction of the magnetic flux causes the stator to vibrate, thereby transmitting vibration to the motor structure and radiating noise to the air. The frequency and amplitude of this radial electromagnetic force wave have a significant effect on the vibration of the motor.

B. Mathematical Model of Radial Electromagnetic Force

According to the Maxwell tensor method, the radial electromagnetic force per unit area of the inner surface of the stator can be calculated as [21]

$$\sigma_r(\theta,t) = \frac{b^2(\theta,t)}{2\mu_0} \tag{1}$$

where θ is the stator reference angle, t is time, μ_0 is vacuum permeability and its value is $4\pi \times 10^{-7}\mathrm{H/m}$, and b is air-gap flux density.

Multiplying magneto motive force (MMF) by air-gap permeance, the air gap magnetic density b can be expressed as

$$b(\theta,t) = f(\theta,t)\,\lambda(\theta,t) \tag{2}$$

where $f(\theta,t)$ is the MMF of air gap, and $\lambda(\theta,t)$ is the air-gap permeance.

When the IPMSM is driven by a voltage source inverter, the MMF of air gap is expressed as

$$f(\theta,t) = f_\mu(\theta,t) + f_o(\theta,t) + f_v(\theta,t) + f_h(\theta,t) \tag{3}$$

where $\mu, o, v,$ and h are spatial orders of the normal electromotive force. Correspondingly, $f_\mu(\theta,t)$ is the MMF caused by permanent magnets, $f_o(\theta,t)$ is the fundamental MMF caused by the

stator fundamental current, $f_v(\theta,t)$ is the harmonic MMF caused by the stator fundamental current, $f_h(\theta,t)$ is the harmonic MMF caused by the h time harmonic current. These MMFs can be written as follows:

$$f_0(\theta,t) = F_0\cos(p\theta - \omega_0 t - \varphi_0) \tag{4}$$

$$f_v(\theta,t) = \sum_v F_v\cos(v\theta - \omega_0 t - \varphi_1) \tag{5}$$

$$f_\mu(\theta,t) = \sum_\mu F_\mu\cos(\mu\theta - \mu\omega_0 t/p - \varphi_2) \tag{6}$$

$$f_h(\theta,t) = \sum_h F_h\cos(h\theta - h\omega_0 t - \varphi_3). \tag{7}$$

The air-gap permeance can be expressed as

$$\lambda(\theta,t) = \Lambda_0 + \sum_k \lambda_k \tag{8}$$

where Λ_0 is the invariant part of the air-gap permeance per unit area, λ_k is the periodic component of the air-gap permeance, and it can be written as

$$\lambda_k = \Lambda_k \sum_k \cos(kz\theta) \qquad k = 1,2,3,\ldots \tag{9}$$

where z is the number of stator slots.

Therefore, according to (1)–(9), the radial electromagnetic force is obtained as (10), shown at the bottom of this page, where some functions, such as $G_v, G_{\mu,m}, G_{\mu,m,h}$, and so on, are defined to express the radial electromagnetic force components.

For integer slot IPMSMs, the relationship between p and v, μ are

$$v = (2nk_1+1)p, \quad k_1 = 0,\pm1,\pm2,\ldots \tag{11}$$

$$\mu = (2k_2+1)p, \quad k_2 = 0,1,2,\ldots \tag{12}$$

where n is the number of phases. Further frequencies in (10) become

$$\left(\frac{\mu}{p}\pm1\right)f_0 = 2k_2 f_0 \tag{13}$$

$$(h\pm1)f_o = af_c \pm bf_0 \tag{14}$$

$$\left(h\pm\frac{\mu}{p}\right)f_o = cf_c \pm df_0 \pm (2k+1)f_0. \tag{15}$$

TABLE I
COMPONENT, ORDER, AND FREQUENCY OF NORMAL ELECTROMAGNETIC FORCE

Component	Order	Frequency
G_0	$2p$	$2f_o$
G_v	$p\pm v = 0/\geq 2p$	$2f_o$
G_μ	$p\pm\mu = 0/\geq 2p$	$\left(\frac{\mu}{p}\pm1\right)f_o$
G_h	$p\pm v = 0/\geq 2p$	$(h\pm1)f_o$
G_m	$2p\pm mz > 2p$	$2f_o$
$G_{\mu,m}$	$\pm mz + p \pm \mu$	$\left(\frac{\mu}{p}\pm1\right)f_o$
$G_{\mu,v}$	$v\pm\mu$	$\left(\frac{\mu}{p}\pm1\right)f_o$
$G_{v,h}$	$2v\geq 2p$	$(h\pm1)f_o$
$G_{v,m}$	$\pm mz + p \pm v$	$2f_o$
$G_{v,\mu,m}$	$\pm mz + v \pm \mu$	$\left(\frac{\mu}{p}\pm1\right)f_o$
$G_{\mu,h}$	$v\pm\mu$	$\left(h\pm\frac{\mu}{p}\right)f_o$
$G_{m,h}$	$\pm mz \pm p + v$	$(h\pm1)f_o$
$G_{\mu,m,h}$	$\pm mz \pm \mu + v$	$\left(h\pm\frac{\mu}{p}\right)f_o$

Considering the aforementioned situation comprehensively, Table I presents the expression of the order and frequency of the radial electromagnetic force generated by the IPMSM.

Only radial electromagnetic forces with low vibration orders and large vibration amplitudes play major roles in the vibration and noise of the motor, so radial electromagnetic forces with high vibration orders and small vibration amplitudes can be simplified. Therefore, the radial electromagnetic force represented by the expression (10) mainly includes the following parts:

1) vibration force wave generated by fundamental wave of magnetic field (G_0, order $= 2p$, frequency $= 2f_0$);
2) vibration force waves generated by the interaction of the stator harmonic magnetic field and the rotor harmonic magnetic field ($G_{v,\mu}$, order $= 0$ or $\geq 2p$, frequency $= 2k_2 f_0$);
3) radial electromagnetic excitation force wave generated by IPMSM powered by frequency converter (G_h, $G_{\mu,h}$, $G_{m,h}$, $G_{\mu,m,h}$, order $= 0$ or $\geq 2p$, frequency $= f_c \pm k_3 f_0$ or $2f_c \pm k_4 f_0$, k_3 is odd and k_4 is even in this article).

$$\begin{aligned}
\Theta_r \cong\ & \frac{1}{2\mu_0}\times\left\{\begin{array}{l} F_0\Lambda_0\cos(p\theta-\omega_0 t-\varphi_0)+\Lambda_0\sum_v F_v\cos\left(v\theta-\omega_0 t-\varphi_1\right)+\Lambda_0\sum_\mu F_\mu\cos\left(\mu\theta-\frac{\mu}{p}\omega_0 t-\varphi_2\right) \\ +\Lambda_0\sum_\mu F_\mu\cos\left(\mu\theta-\frac{\mu}{p}\omega_0 t-\varphi_2\right)+\Lambda_0\sum_h F_h\cos(v\theta-h\omega_0 t-\varphi_3)+\frac{F_0}{2}\sum_m\Lambda_m\cos\left[(p\pm mz)\theta-\omega_0 t-\varphi_0\right] \\ +\frac{1}{2}\sum_\mu\sum_m F_\mu\Lambda_m\cos\left[(\mu\pm mz)\theta-\frac{\mu}{p}\omega_0 t-\varphi_2\right]\end{array}\right\}^2 \\
=\ & \frac{F_0^2\Lambda_0^2}{4\mu_0}\left[\cos(2p-2\omega_0 t-2\varphi_0)+1\right]+G_v\langle(p\pm v)\theta,2f_0\rangle+G_\mu\left\langle(p\pm\mu)\theta,\left(\frac{\mu}{p}\pm1\right)f_0\right\rangle+G_m\langle(2p\pm mz)\theta,2f_0\rangle \\
& +G_{\mu,m}\left\langle(p\pm\mu\pm mz)\theta,\left(\frac{\mu}{p}\pm1\right)f_0\right\rangle+G_{\mu,v}\left\langle(v\pm\mu)\theta,\left(\frac{\mu}{p}\pm1\right)f_0\right\rangle+G_{m,v}\langle(p\pm v\pm mz)\theta,2f_0\rangle \\
& +G_{m,\mu,v}\left\langle(\pm m+\mu\pm v)\theta,\left(\frac{\mu}{p}\pm1\right)f_0\right\rangle+G_h\langle(p\pm v)\theta,(h\pm1)f_0\rangle+G_{v,h}\langle 2v\theta,(h\pm1)f_0\rangle \\
& +G_{\mu,h}\left\langle(\mu\pm v)\theta,\left(h\pm\frac{\mu}{p}\right)f_0\right\rangle+G_{m,h}\langle(v\pm p\pm mz)\theta,(h\pm1)f_0\rangle+G_{\mu,m,h}\left\langle(v\pm\mu\pm mz)\theta,\left(h\pm\frac{\mu}{p}\right)f_0\right\rangle
\end{aligned} \tag{10}$$

It can be seen that there are six kinds of radial electromagnetic force components. Among them, the electromagnetic force component generated by the fundamental wave magnetic field and the stator harmonic magnetic field has no relationship with the h-order time harmonic currents and the frequency is low. However, another radial electromagnetic force component with high frequency, small order, and large amplitude is a key part, and this force is generated by the interaction between the fundamental magnetic field of the stator generated by the h-order harmonic and the fundamental magnetic field of the rotor permanent magnet. Therefore, this part of force will significantly affect the vibration and noise of the motor, and it is an important aspect of studying the characteristics of motor vibration and noise under different driving strategies.

C. Influence of Control Strategy on Radial Electromagnetic Force

In the Appendix, (10) is more fully presented as (24). It can be observed that

$$G_0 = \frac{F_0^2 \Lambda_0^2}{4\mu_0} \left[\cos\left(2p - 2\omega_0 t - 2\varphi_0\right) + 1\right]. \tag{16}$$

In addition

$$F_0 = F_{s,1}(\theta, t) + F_{r,1}(\theta, t) \tag{17}$$

where $F_{s,1}(\theta, t)$ and $F_{r,1}(\theta, t)$ are the fundamental magnetomotive force of the stator and rotor, respectively. According to the theory of synchronous motors, the amplitude of the stator fundamental magnetomotive force is

$$F_{s,1} = \frac{M\sqrt{2}}{\pi p} \mathrm{N} k_{N1} I \tag{18}$$

and the currents of the three-phase windings are

$$\begin{aligned} i_A &= \sqrt{2} I \cos(\omega t + \varphi) \\ i_B &= \sqrt{2} I \cos\left(\omega t - \frac{2\pi}{3} + \varphi\right) \\ i_C &= \sqrt{2} I \cos\left(\omega t - \frac{4\pi}{3} + \varphi\right). \end{aligned} \tag{19}$$

The different control strategies cause the current characteristics (I, φ) of the motor to be different. Therefore, the stator fundamental magnetomotive forces $(F_{s,1})$ are different, which will lead to different radial force fundamental components of radial force (G_0).

Similarly, the force components generated by the interaction of the stator harmonic magnetic field and the rotor harmonic magnetic field are expressed as

$$\begin{aligned} G_{v,\mu} = &\frac{\Lambda_0^2}{2\mu_0} \sum_{\nu} \sum_{\mu} F_\nu F_\mu \\ &\times \left\{ \begin{aligned} &\cos\left[(\nu + \mu)\theta - \left(1 + \tfrac{\mu}{p}\right)\omega_0 t - \varphi_{12}\right] \\ &+ \cos\left[(\nu - \mu)\theta - \left(1 - \tfrac{\mu}{p}\right)\omega_0 t - \varphi_{21}\right] \end{aligned} \right\} \end{aligned} \tag{20}$$

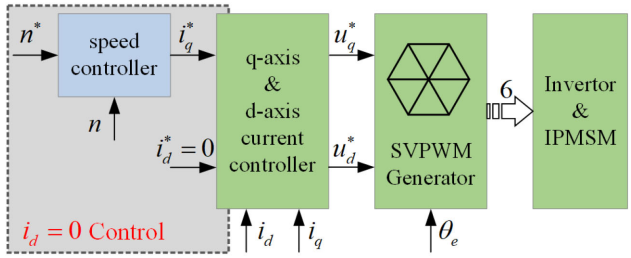

Fig. 2. Control block diagram of the i_d=0 control algorithm.

and

$$F_v = \frac{M\sqrt{2}}{\pi v p} \mathrm{N} k_{N1} I_v. \tag{21}$$

Therefore, when the control strategies are different, the amplitude of magnetomotive force at the same harmonic order will be different due to the different currents.

According to the same influence mechanism, the components G_h, $G_{\mu,h}$, $G_{m,h}$, and $G_{\mu,m,h}$ of the radial electromagnetic force are also affected by the control strategies.

III. FOC Control Method and Electromagnetic Force of IPMSM

A. $i_d = 0$ Control Algorithm

To facilitate the FOC control, researchers proposed $i_d = 0$ control algorithm. In this algorithm, the d-axis current has to be kept at zero regardless of the magnitude of the q-axis current. Then, the torque is controlled by varying the value of the q-axis current, as shown in Fig. 2. The computed torque is

$$T_e = \frac{3p}{2} \Psi_m i_{\mathrm{sq}}. \tag{22}$$

The structure of this algorithm is simple, and this system has good torque control performance and a wide speed range. However, in order to ensure that the speed control system has sufficient power supply voltage under heavy load, the inverter needs to have a sufficient voltage margin. When the load increases, the power factor decreases, and the output torque capability is low.

B. MTPA Control Algorithm Based on LUT Method

The MTPA control methods based on offline LUTs were proposed to improve the output torque capability and a typical control block is shown in Fig. 3. In this method, the stator current with a certain amplitude produces the largest torque. In other words, this algorithm can produce a certain electromagnetic torque by the use of the smallest stator current, which contributes to relatively lower copper loss. Compared with the $i_d = 0$ control method, for the same torque, the stator current of this control method is much smaller. This control method significantly reduces the supply voltage of the stator and improves the operating efficiency of the motor. The MTPA control method based on LUT is computationally intensive. However, this method increases the workload of offline measurements. Besides, the

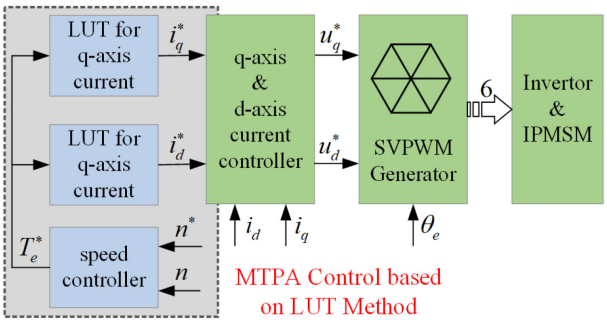

Fig. 3. Control block diagram of the MTPA control algorithm based on LUT.

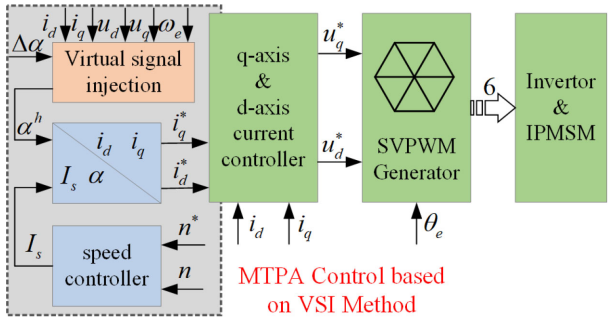

Fig. 5. Control block diagram of the MTPA control algorithm based on VSIM.

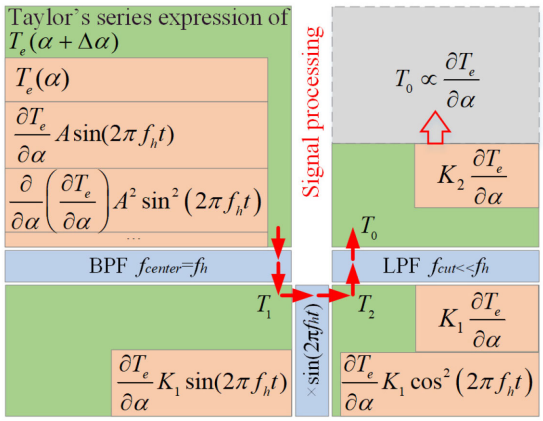

Fig. 4. Signal processing scheme.

LUTs require additional storage resources. Therefore, the online MTPA control method is expected.

C. MTPA Control Algorithm Based on Visual Signal Injection Method

Instead of distributing the d-axis and q-axis current commands based on offline LUTs, an online MTPA control

$$\alpha^h = \alpha + \Delta\alpha = \alpha + A\sin(2\pi f_h t) \tag{23}$$

is injected to the measured stator current angle mathematically, where A and f_h are the magnitude and the frequency of the injected signal, respectively.

Then, the corresponding calculated electromagnetic torque is also injected to the high-frequency disturbance and the proportional term of torque derivative is obtained through various filters, as shown in Fig. 4. If the value of this proportional term is controlled to zero, the MTPA angle is generated. The control block diagram of this algorithm is shown in Fig. 5.

All processes of this strategy are based on the mathematical level, so there is no real signal injected into the IPMSM. The advantages of this strategy are that it retains timeliness and parameter independence while eliminating additional copper loss and additional torque vibration.

TABLE II
MAIN PARAMETERS OF THE TEST IPMSM

Parameters	Values
Air-gap length	1 mm
Number of pole pairs	3
Number of slots	36
Number of phases	3
Rated power	7.5 kW
Rated speed	3000 rpm

D. Analysis of Electromagnetic Force Harmonics Under Different Control Algorithms

To investigate the force harmonics, the electromagnetic forces are generated in a test motor. This motor is an IPMSM drove by different control algorithms, and Table II summarizes the parameters of this tested IPMSM.

Figs. 6 and 7 show the spatial distribution and the frequency map of radial electromagnetic force density under different control algorithms. The speed was varied from 500 (low speed) up to 3000 r/min (high speed), the load torque is 10 N·m, and the switching frequency is 7.5 kHz.

It is noted that, with the $i_d = 0$ control strategy, the peak value of the radial electromagnetic force in spatial distribution map will be slightly larger than the MTPA control strategies. The VSIM-based MTPA strategy is slightly lower than the LUTM-based MTPA control strategy. In addition, the frequencies of the fundamental forces under these three working conditions are 25 Hz, 75 Hz and 150 Hz, respectively. From Fig. 7, two types of force harmonics are divided. The first type is force harmonics which are $2k_2$ times the fundamental frequency; and the second type of force harmonics are closely related to the switching frequency. It can be seen that in the first type of force harmonics, major components are the harmonic generated by fundamental wave of magnetic field $(2f_0)$ and the harmonics caused by rotor poles, such as $4f_0, 6f_0, 8f_0$, and so on. Moreover, for these three control methods, the frequency points of the force peak are very close at any speed. However, it is obvious that, in the MTPA control mode, the force at $2f_0$ has increased, and this phenomenon is due to the efficiency advantage of the MTPA control strategy. For the second type of force harmonics, the frequencies are equal to $f_c \pm k_3 f_0$ and $2f_c \pm k_4 f_0$. It also found that near f_c, the frequency distributions and amplitudes

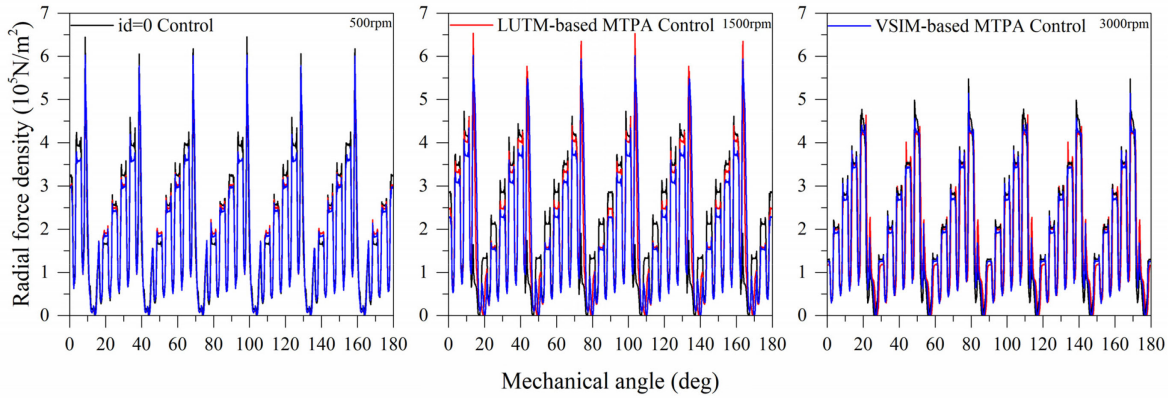

Fig. 6. Spatial distribution of electromagnetic force density under different control algorithms.

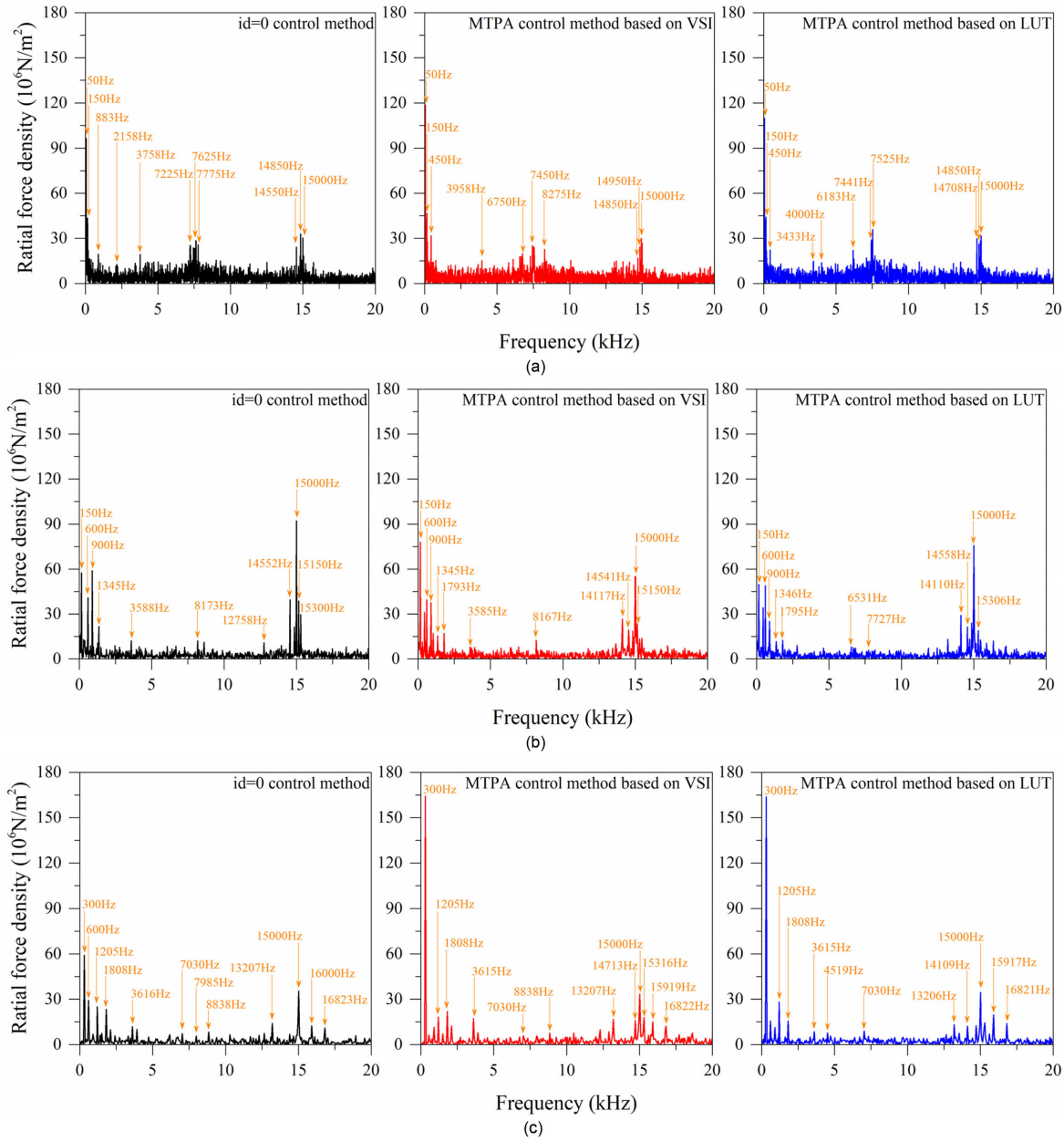

Fig. 7. Frequency map of electromagnetic force density under different control algorithms. (a) Speed is 500 r/min. (b) Speed is 1500 r/min. (c) Speed is 3000 r/min.

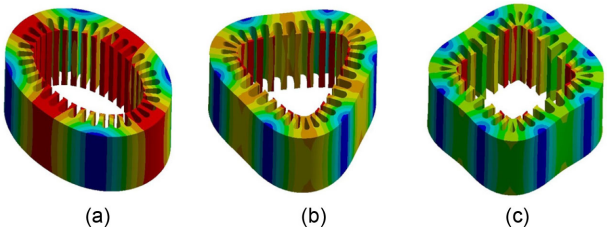

Fig. 8. Modal shapes and frequencies of the stator. (a) 1203 Hz. (b) 2811 Hz. (c) 4110 Hz.

of the harmonics are close. However, near $2f_c$, the amplitudes of MTPA control based on VSIM and LUTM are smaller than those of the $i_d = 0$ control method, especially VSIM has the most obvious effect.

In conclusion, the frequency of fundamental magnetic field in 50–300 Hz, the natural frequencies in 1000–4000 Hz, the frequencies near $f_c \pm 2f_0$ and $2f_c \pm f_0$ influence electromagnetic force density practically. Considering that the resonance frequencies will not change significantly with the control strategies when the structure of system is unchanged, the frequency of fundamental magnetic field in 50–300 Hz, the frequencies near $f_c \pm 2f_0$ and $2f_c \pm f_0$ are significant for comparative analysis.

IV. Prediction of Vibration and Noise Considering Different Control Algorithms

A. Structural Modal Analysis of Stator

For an IPMSM, it is very important to investigate the low-order natural frequencies and their modes of the stator for reducing the noise [28]. Then, distributions of the frequencies and their modes can effectively optimize the control strategies. Most harsh noises are generated when the natural frequency of the stator coincides with or is close to the frequency of the magnetomotive force [29]. Therefore, the natural frequencies of the stator core and stator assembly must be predicted at the beginning of the design to reduce electromagnetic noise.

To predict the natural frequencies and their modes of the stator, a model of stator core, which is laminated by silicon steel sheets and the teeth are wound by coils, is built. Then, this stator core and casing constitute the stator assembly. As a consequence, the first three modal frequencies of the stator assembly are 1203, 2811, and 4110 Hz respectively. Fig. 8 shows the modal shapes and frequencies of the stator.

B. Description of the Test Platform

In this article, the experiment can only observe vibration and noise, and the characteristics of radial force mainly come from mathematical calculations and FEM analysis. Fig. 9 shows the schematic plot of the noise test. This system is independent in an environment without outside noise. The test object is an IPMSM, which is employed in a small EV. The motor shaft is connected with the dynamometer by a coupling and the motor is located in a locating frame by eight screws. The locating frame is firmly connected to the pedestals. The vibration sensor for observation is fixed on the outer surface of the motor casing. A Bluetooth

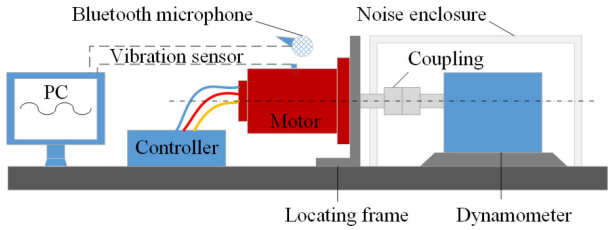

Fig. 9. Schematic plot of the test platform.

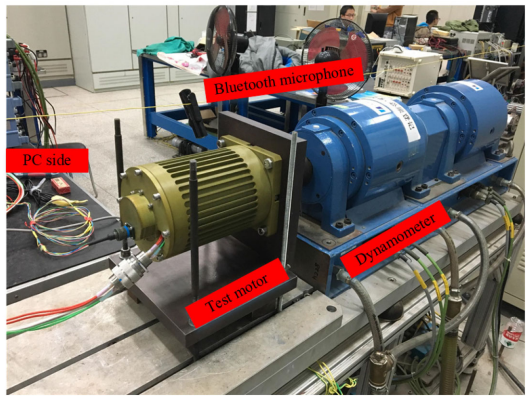

Fig. 10. Experiment platform for testing the acoustic noise.

microphone is suspended 20 cm above the motor using a rubber band, which can transmit the noise waveform and data of the motor in real time to the computer. Meanwhile, the dynamometer is covered by a noise enclosure to isolate the noise. Fig. 10 shows the corresponding experiment platform for testing the acoustic noise.

C. Comparison of Electromagnetic Vibration

The motor being analyzed is a rotating PMSM with V-type embedded permanent magnets, 6 poles, 36 slots, and double-layer windings. The PMSM is a fully axially symmetric structure and the electromagnetic force distributes uniformly in the axial direction; therefore, a 2-D sectioning model of the PMSM is sufficient to accurately demonstrate the structural and electromagnetic characteristics. The main parameters of the PMSM are shown in Table II. The nodal forces acting on the stator can be calculated. Then, the electromagnetic forces of 3-D model can be obtained according to the axial symmetry of the model.

In order to improve the calculation accuracy, the electromagnetic forces are loaded at the surface of each stator tooth. Then, the stator surface vibration is calculated and the results based on three different control algorithms are compared.

Fig. 11 shows the comparison of acceleration and equivalent radiated power level of radial vibration. It can be seen that the main vibration peaks are distributed in three frequency regions. The most significant vibration band is close to the switching frequency and these vibration frequencies contain $f_c \pm f_0$, $f_c \pm 2f_0$, $f_c \pm 3f_0$, and so on. In low-frequency band, vibration peaks appear at 1500, 3850, and 5400 Hz, which are resonance frequencies of the stator assembly. In high-frequency band, dominant vibration peak appear at 15 000 Hz ($2f_c$), which is induced by time harmonics due to switching frequency.

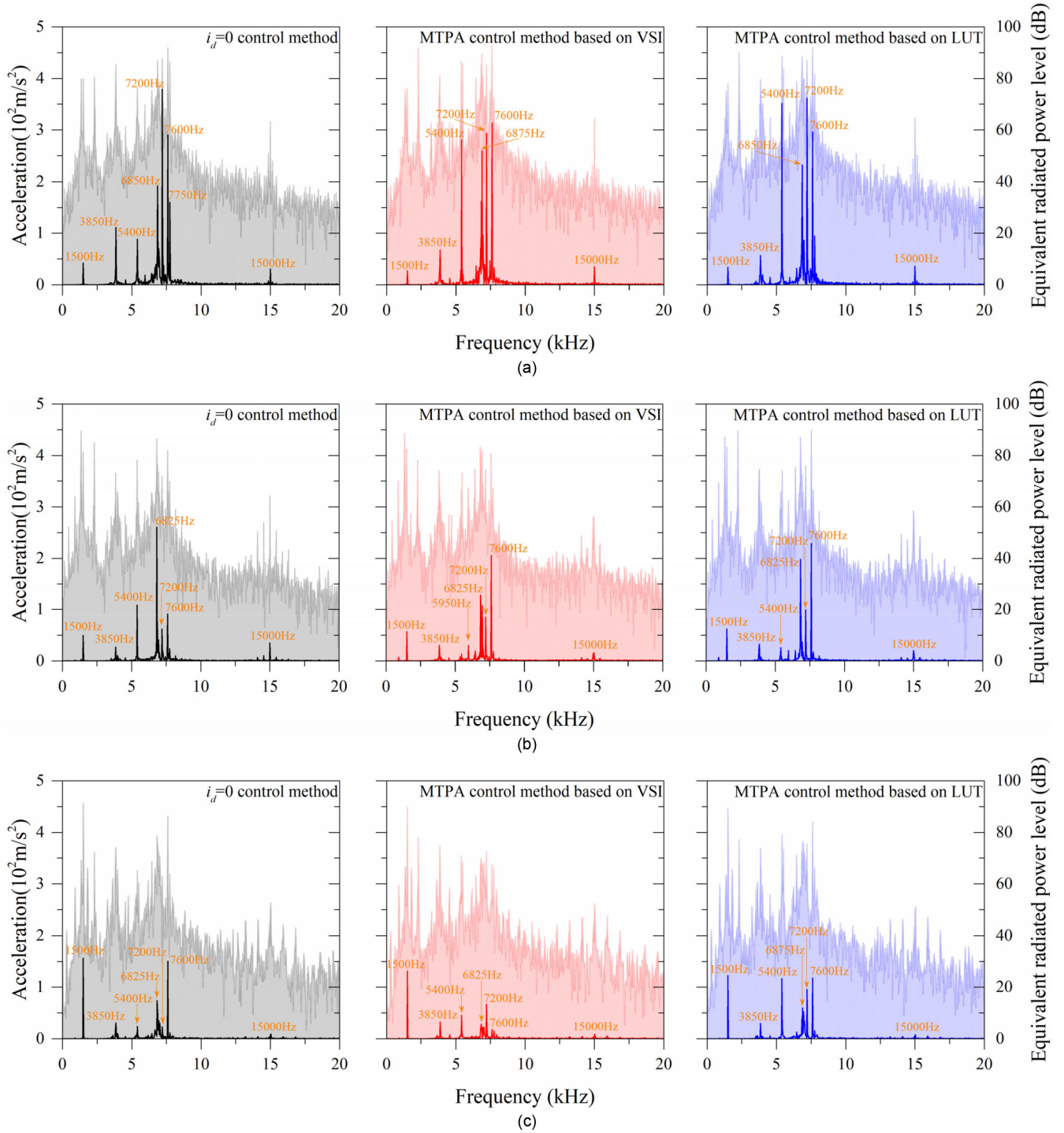

Fig. 11. Acceleration and equivalent radiated power level of radial vibration. (a) Speed is 500 r/min. (b) Speed is 1500 r/min. (c) Speed is 3000 r/min.

The comparison results show that, in the frequency band close to the switching frequency, the vibration caused by MTPA control based on VSIM is the slightest, and the vibration caused by $i_d = 0$ control method is the most severe.

D. Comparison of Electromagnetic Noise

This test IPMSM control system must be rigidly installed to avoid introducing additional mechanical vibration and noise sources. When the motor operates at 500, 1500, and 3000 r/min without load, the noises of the motor are measured and the comparison of sound pressure level is shown in Fig. 12.

In Fig. 12, through some peak values, the inherent noise frequency characteristics of the system are fully displayed, including low-frequency noise of the mechanical structure, the resonance frequency noises (near 1650 Hz, 2580 Hz, and 4190 Hz), the switching frequency noise near 7500 Hz and 15000 Hz.

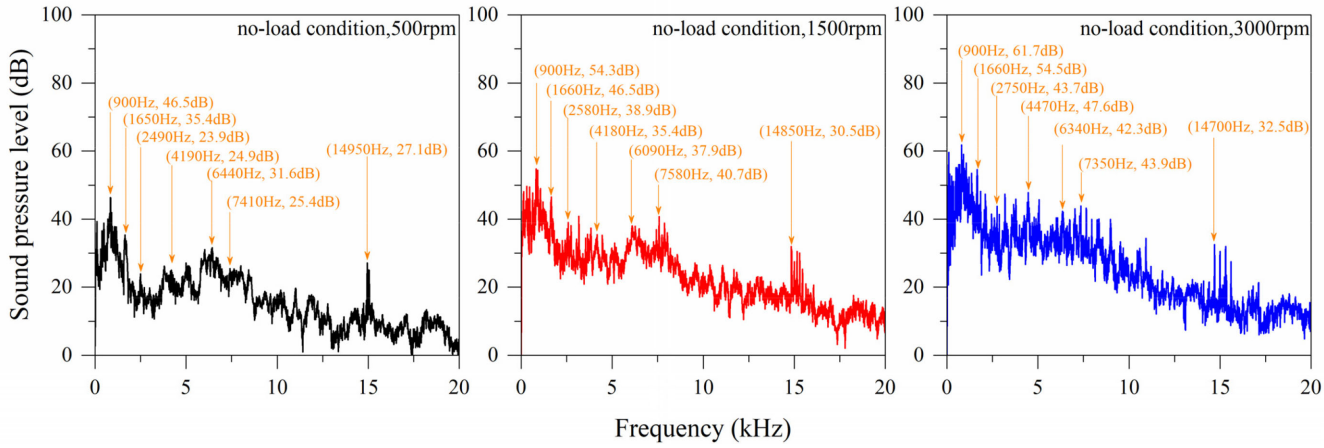

Fig. 12. Sound pressure level of IPMSM without load.

When the motor runs with load, these frequency components are very significant for comparative analysis.

When the motor operates at 500, 1500, and 3000 r/min under a load torque of 10 N·m, the noises of the motor are measured and the comparison of sound pressure level is shown in Fig. 13. The comparison of noise is from test motor controlled by the previous three strategies. It can be seen that the frequency domain waveform can detail the SPL of the motor noise at each frequency. Moreover, in low-frequency band, main SPL peaks are very significant, which are produced by a mechanical structure. Therefore, the noise in this frequency band is more closely related to the physical structure of the motor. And the difference is mainly caused by the resonance degree between the different fundamental frequency and the natural frequency. In this low-frequency band, it is found that the frequency distribution of the SPL peak point changes little when the control method changes at the same speed. The noise harmonics near the switching frequency is the main noise in the middle frequency band, and this part of harmonics is closely related to the switching frequency. Compared with the noise harmonics in the low-frequency band, these harmonics are sensitive to the control strategies of, and they can cause motor howling. Fig. 13 shows that the MTPA control methods can weaken the SPL mid-frequency amplitude, and the effect of VSIM is very obvious. It is also found that the dominant peaks in the high-frequency band are concentrated around the twice switching frequency and the amplitude of these harmonics can also be changed by the control strategies. Similarly, in the high-frequency band, the MTPA control methods can still play a very positive role to reduce noise.

V. Explanation of Noise in IPMSM Controlled by Different Algorithms

When the test IPMSM is controlled by the three strategies separately, the main noise peaks and frequencies generated by the motor in low-frequency band are basically the same, but the main noise peak and frequency generated in middle- and high-frequency bands are quite different.

TABLE III
Noise Peaks of the Test IPMSM From 0 to 5 kHz

Speed (rpm)	i_d=0		VSI		LUT	
	Frequency (Hz)	SPL (dB)	Frequency (Hz)	SPL (dB)	Frequency (Hz)	SPL (dB)
500	120	51.0	120	54.0	120	54.1
	300	56.4	300	58.0	300	59.2
	900	52.2	900	47.2	850	55.7
	3000	37.0	3000	24.6	3000	22.8
1500	130	64.7	130	65.1	130	64.2
	300	61.4	300	58.8	300	59.3
	910	59.9	910	58.2	900	61.5
	2700	41.0	2700	42.5	2540	43.3
	4200	34.7	4200	34.5	4200	41.8
3000	100	74.8	100	76.8	100	74.1
	300	69.9	300	74.0	300	69.6
	930	76.8	930	75.6	930	75.8
	2690	55.1	2680	54.2	2570	53.2

In the low-frequency band, the frequencies corresponding to the noise peaks are shown in Table III.

Low-frequency noise of 120, 300, and 900 Hz is caused by the mechanical system of the test motor. At the same speed, three different control strategies can hardly change this part of noise. However, 2680, 2690, 2700, and 3000 Hz are very close to the modal frequencies of the stator assembly of the test motor. Thus, structural resonance is the main reason for this part of the noise peaks. In general, in the low-frequency field, when the speed is low, the noises caused by the three control strategies are not significantly different. But as the speed increases, the single-point noises caused by the two MTPA control strategies are slightly reduced.

In the middle-frequency band, the frequencies corresponding to the noise peaks are shown in Table IV.

It is found in Table IV that the noise peaks appear at 7050, 7350, 7420, 7530, 7650 Hz, etc. Moreover, these frequencies are close to switching frequency; so, the corresponding noise peaks are caused by the interaction of the fundamental magnetic field generated by the stator time harmonic current and the fundamental magnetic field of the rotor permanent magnet. The comparison of noise peaks in this frequency band shows that the

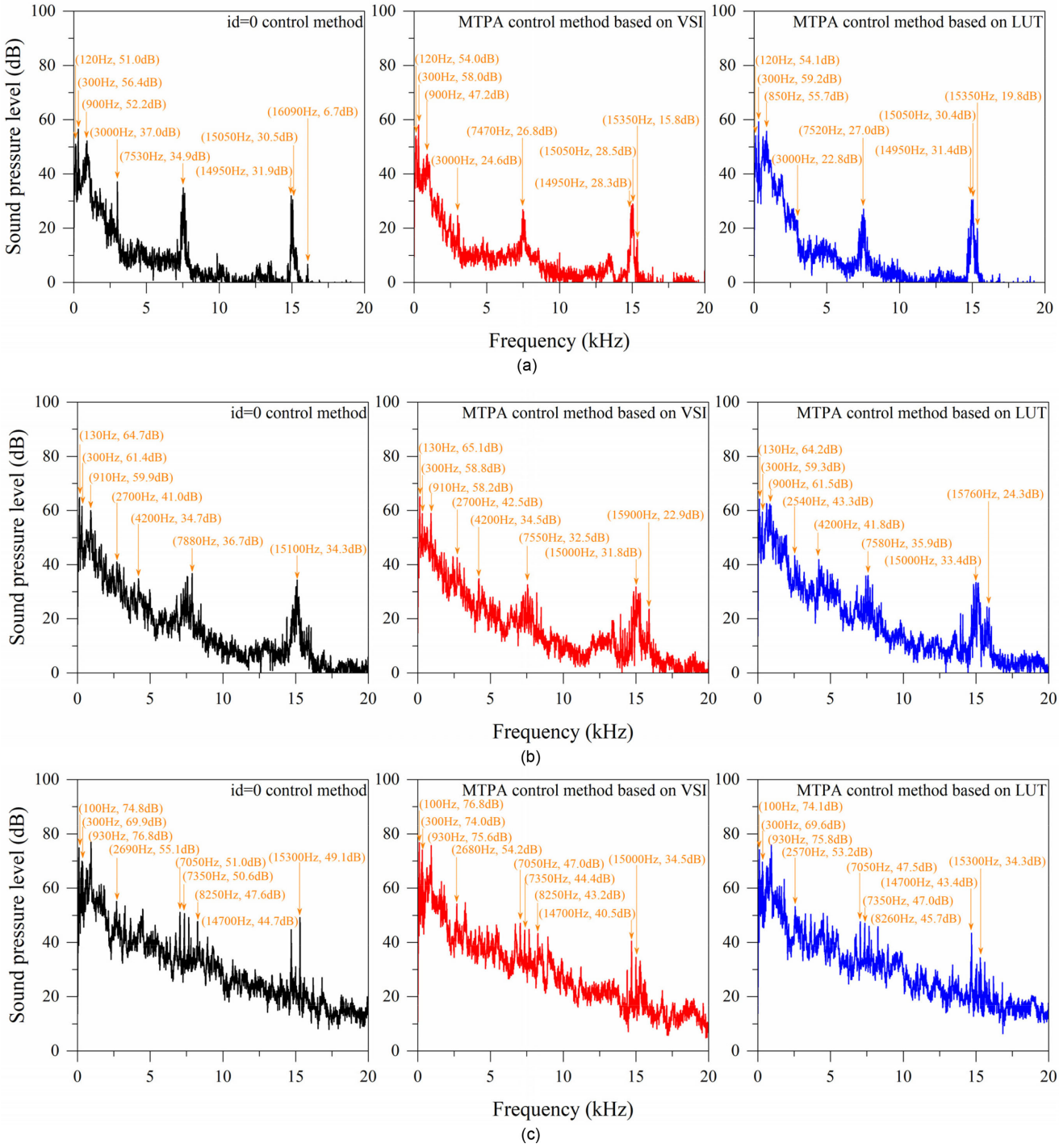

Fig. 13. Sound pressure level of noise. (a) Speed is 500 r/min. (b) Speed is 1500 r/min. (c) Speed is 3000 r/min.

noise of the test IPMSM driven by the MTPA control method based on VSI is the smallest, and the maximum noise peak value is 7.8%–23.2% (varies with speed) lower than that of $i_d = 0$ control method.

In the high-frequency band, the frequencies corresponding to the noise peaks are shown in Table V.

It can be seen that, at 14 700, 15 000, and 15 300 Hz, the noise peaks increase the sound sharpness. These harmonics are close to the twice switching frequency and caused by the interaction between the second harmonic magnetic field generated by the stator current time harmonic and the fundamental magnetic field of the rotor permanent magnet. The comparison results show that, in this frequency band, the MTPA control method based on VSI is most beneficial to reduce noise, and the maximum noise peak value is 7.3% to 17.5% (varies with speed) lower than that of $i_d = 0$ control method.

TABLE IV
NOISE PEAKS OF THE TEST IPMSM FROM 5 TO 10 kHz

Speed (rpm)	i_d=0		VSI		LUT	
	Frequency (Hz)	SPL (dB)	Frequency (Hz)	SPL (dB)	Frequency (Hz)	SPL (dB)
500	7480	32.1	7420	23.3	7420	25.0
	7530	34.9	7470	26.8	7520	27.0
	7630	32.9	7520	26.1	7580	23.8
1500	7420	33.4	7400	29.9	7430	35.8
	7550	35.6	7550	32.5	7580	35.9
	7880	36.7	8180	29.5	7880	32.6
3000	7050	51.0	7050	47.0	7050	47.5
	7350	50.6	7350	44.4	7350	47.0
	7650	49.2	7650	44.7	7650	45.9
	8250	47.6	8250	43.2	8260	45.7

TABLE V
NOISE PEAKS OF THE TEST IPMSM FROM 10 TO 20 kHz

Speed (rpm)	i_d=0		VSI		LUT	
	Frequency (Hz)	SPL (dB)	Frequency (Hz)	SPL (dB)	Frequency (Hz)	SPL (dB)
500	14950	31.9	14950	28.3	14950	31.4
	15050	30.5	15050	28.5	15050	30.4
	15300	12.7	15350	15.8	15350	19.8
1500	14980	28.5	14850	29.9	14850	32.6
	15030	31.9	15000	31.8	15000	33.4
	15100	34.3	15150	29.2	15150	33.2
3000	14700	44.7	14700	40.5	14700	43.4
	15000	31.0	15000	34.5	15000	31.9
	15300	49.1	15300	33.1	15300	34.3

TABLE VI
COMPARISON OF CONTROL CHARACTERISTICS

Method	The difficulty of realization	Copper loss	Effectiveness
i_d=0	Low	High	Low
LUTM-based MTPA	High	Low	High
VSIM-based MTPA	Medium	Low	High

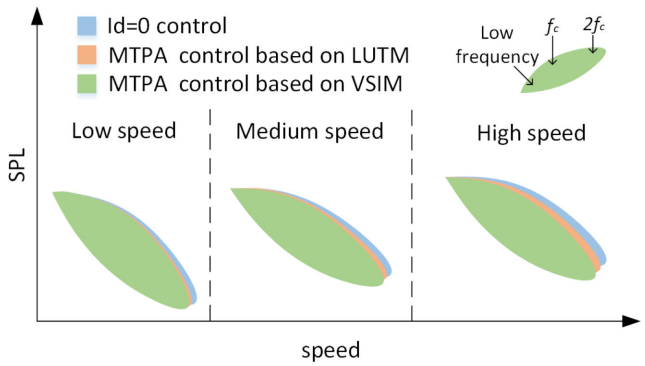

Fig. 14. Comparison of sound pressure level distribution in IPMSM driven by three control strategies.

In order to better clarify the guiding value of the abovementioned research in the assisted system applications, the characteristics of the IPMSMs driven by the three control strategies are further compared in Table VI and Fig. 14.

It can be seen that $i_d = 0$ control strategy is easy to implement with the high copper loss and low efficiency, which is not conducive to temperature rise. Then, the noise is large. The LUTM-based control strategy takes a lot of time to obtain an accurate LUT, which is not easy to implement. However, when the LUT is sufficiently comprehensive and accurate, the copper loss will be low and the efficiency will be high enough. Then, the noise is much better than $i_d = 0$ control. The VSIM-based control strategy is also easy to implement, with low copper loss and high efficiency. The most important thing is that noise characteristics are much better than $i_d = 0$ control.

VI. CONCLUSION

This article analyzes and compares in detail the electromagnetic vibration and noise characteristics of the IPMSM when driven by two MTPA control and $i_d = 0$ control strategies. As a result, the following conclusions are drawn in this article.

1) The influence of control algorithms on vibration and noise are discussed. Compared with the traditional $i_d = 0$ control strategy, the two MTPA control strategies do not introduce additional vibration and noise frequencies, but can reduce vibration and noise peaks. Moreover, the vibration and noise of IPMSM caused by MTPA control based on the VSI method are slightly smaller than those of MTPA control based on the LUT method. It is also noted that when the speed is low, the vibration and noise characteristics caused by these three control strategies are similar. As the speed increases, the vibration and noise of the IPMSM driven by MTPA control based on the VSI method are significantly lower than that of $i_d = 0$ control method.
2) MTPA control strategy, especially MTPA control based on VSI strategy, can be used to improve the efficiency of IPMSMs for EVs. Moreover, this article focuses on the noise characteristics of these control strategies. According to the research, in practical applications, MTPA control based on the VSI method can be utilized to improve efficiency while suppressing noise of IPMSM. Moreover, the suppression effect is different under different operating conditions. From a control point of view, it provides a detailed guide for seeking low-vibration and low-noise motor systems for EVs.

APPENDIX

Each component in (10) can be fully expressed as the following equation:

$$
\begin{aligned}
\Theta_r \cong\ & \tfrac{1}{2\mu_0} \times \left\{ \begin{array}{l} F_0\Lambda_0 \cos\left(p\theta - \omega_0 t - \varphi_0\right) + \Lambda_0 \sum\limits_{\nu} F_\nu \cos\left(\nu\theta - \omega_0 t - \varphi_1\right) + \Lambda_0 \sum\limits_{\mu} F_\mu \cos\left(\mu\theta - \tfrac{\mu}{p}\omega_0 t - \varphi_2\right) \\ +\Lambda_0 \sum\limits_{h} F_h \cos\left(\nu\theta - h\omega_0 t - \varphi_3\right) + \tfrac{F_0}{2} \sum\limits_{m} \Lambda_m \cos\left[\left(p \pm mz\right)\theta - \omega_0 t - \varphi_0\right] \\ +\tfrac{1}{2} \sum\limits_{\mu} \sum\limits_{m} F_\mu \Lambda_m \cos\left[\left(\mu \pm mz\right)\theta - \tfrac{\mu}{p}\omega_0 t - \varphi_2\right] \end{array} \right\} \\
=\ & \tfrac{F_0^2\Lambda_0^2}{4\mu_0}\left[\cos\left(2p - 2\omega_0 t - 2\varphi_0\right) + 1\right] + \tfrac{\Lambda_0^2}{4\mu_0} \sum_{\nu_1} \sum_{\nu_2} F_{\nu_1} F_{\nu_2} \left\{ \begin{array}{l} \cos\left[\nu_{12}\theta - 2\omega_0 t - 2\varphi_1\right] \\ +\cos\left[\nu_{21}\theta\right] \end{array} \right\} \\
& + \tfrac{\Lambda_0^2}{4\mu_0} \sum_{\mu_1} \sum_{\mu_2} F_{\mu_1} F_{\mu_2} \left\{ \begin{array}{l} \cos\left[\mu_{12}\theta - \tfrac{\mu_{12}}{p}\omega_0 t - 2\varphi_2\right] \\ +\cos\left[\mu_{21}\theta - \tfrac{\mu_{21}}{p}\omega_0 t\right] \end{array} \right\} + \tfrac{\Lambda_0^2}{4\mu_0} \sum_{h_1} \sum_{h_2} F_{h_1} F_{h_2} \left\{ \begin{array}{l} \cos\left[2\nu\theta - h_{12}\omega_0 t - 2\varphi_3\right] \\ +\cos\left[h_{21}\omega_0 t\right] \end{array} \right\} \\
& + \tfrac{F_0\Lambda_0^2}{2\mu_0} \sum_{\nu} F_\nu \left\{ \begin{array}{l} \cos\left[\left(p + \nu\right)\theta - 2\omega_0 t - \varphi_{01}\right] \\ +\cos\left[\left(p - \nu\right)\theta - \varphi_{10}\right] \end{array} \right\} + \tfrac{F_0\Lambda_0^2}{2\mu_0} \sum_{\mu} F_\mu \left\{ \begin{array}{l} \cos\left[\left(p + \mu\right)\theta - \left(1 + \tfrac{\mu}{p}\right)\omega_0 t - \varphi_{02}\right] \\ +\cos\left[\left(p - \mu\right)\theta - \left(1 - \tfrac{\mu}{p}\right)\omega_0 t - \varphi_{20}\right] \end{array} \right\} \\
& + \tfrac{F_0\Lambda_0^2}{2\mu_0} \sum_{h} F_h \left\{ \begin{array}{l} \cos\left[\left(p + \nu\right)\theta - \left(1 + h\right)\omega_0 t - \varphi_{03}\right] \\ +\cos\left[\left(p - \nu\right)\theta - \left(1 - h\right)\omega_0 t - \varphi_{30}\right] \end{array} \right\} \\
& + \tfrac{1}{16\mu_0} \sum_{\mu_1} \sum_{\mu_2} \sum_{m_1} \sum_{m_2} F_{\mu_1} F_{\mu_2} \Lambda_{m_1} \Lambda_{m_2} \left\{ \begin{array}{l} 3\cos\left[\begin{array}{l}\left(\mu_{12} + m_{12}z\right)\theta \\ -\tfrac{\mu_{12}}{p}\omega_0 t - 2\varphi_2\end{array}\right] \\ +\cos\left[\begin{array}{l}\left(\mu_{12} - m_{12}z\right)\theta \\ -\tfrac{\mu_{12}}{p}\omega_0 t - 2\varphi_2\end{array}\right] \\ +3\cos\left[\begin{array}{l}\left(\mu_{21} + m_{21}z\right)\theta \\ -\tfrac{\mu_{21}}{p}\omega_0 t\end{array}\right] \\ +\cos\left[\begin{array}{l}\left(\mu_{21} - m_{21}z\right)\theta \\ -\tfrac{\mu_{21}}{p}\omega_0 t\end{array}\right] \end{array} \right\} \\
& + \tfrac{F_0^2}{16\mu_0} \sum_{m_1} \sum_{m_2} \Lambda_{m_1} \Lambda_{m_2} \left\{ \begin{array}{l} \cos\left[\left(2p \pm m_{12}z\right)\theta - 2\omega_0 t - 2\varphi_0\right] \\ +2\cos\left[\left(2p + m_{21}z\right)\theta - 2\omega_0 t - 2\varphi_0\right] \\ +2\cos\left[m_{12}z\theta\right] + 2\cos\left[m_{21}z\theta\right] \end{array} \right\} \\
& + \tfrac{F_0^2\Lambda_0}{4\mu_0} \sum_{m} \Lambda_m \left\{ \begin{array}{l} \cos\left[\left(2p \pm mz\right)\theta - 2\omega_0 t - 2\varphi_0\right] \\ +2\cos\left[\left(mz\right)\theta\right] \end{array} \right\} + \tfrac{F_0\Lambda_0}{2\mu_0} \sum_{\mu} \sum_{m} F_\mu \Lambda_m \left\{ \begin{array}{l} \cos\left[\begin{array}{l}\left(p + \mu \pm mz\right)\theta \\ -\left(1 + \tfrac{\mu}{p}\right)\omega_0 t - \varphi_{02}\end{array}\right] \\ +\cos\left[\begin{array}{l}\left(p - \mu \pm mz\right)\theta \\ -\left(1 - \tfrac{\mu}{p}\right)\omega_0 t - \varphi_{20}\end{array}\right] \end{array} \right\} \\
& + \tfrac{\Lambda_0^2}{2\mu_0} \sum_{\nu} \sum_{\mu} F_\nu F_\mu \left\{ \begin{array}{l} \cos\left[\left(\nu + \mu\right)\theta - \left(1 + \tfrac{\mu}{p}\right)\omega_0 t - \varphi_{12}\right] \\ +\cos\left[\left(\nu - \mu\right)\theta - \left(1 - \tfrac{\mu}{p}\right)\omega_0 t - \varphi_{21}\right] \end{array} \right\} \\
& + \tfrac{\Lambda_0^2}{2\mu_0} \sum_{\nu} \sum_{h} F_\nu F_h \left\{ \begin{array}{l} \cos\left[2\nu\theta - \left(1 + h\right)\omega_0 t - \varphi_{13}\right] \\ +\cos\left[-\left(1 - h\right)\omega_0 t - \varphi_{31}\right] \end{array} \right\} + \tfrac{F_0\Lambda_0}{4\mu_0} \sum_{\nu} \sum_{m} F_\nu \Lambda_m \left\{ \begin{array}{l} \cos\left[\left(p + \nu \pm mz\right)\theta - 2\omega_0 t - \varphi_{01}\right] \\ +\cos\left[\left(p - \nu \pm mz\right)\theta - \varphi_{10}\right] \end{array} \right\} \\
& + \tfrac{F_0\Lambda_0}{4\mu_0} \sum_{h} \sum_{m} F_h \Lambda_m \left\{ \begin{array}{l} \cos\left[\left(\nu + p \pm mz\right)\theta - \left(h + 1\right)\omega_0 t - \varphi_{30}\right] \\ +\cos\left[\left(\nu - p \pm mz\right)\theta - \left(h - 1\right)\omega_0 t - \varphi_{03}\right] \end{array} \right\} \\
& + \tfrac{\Lambda_0}{4\mu_0} \sum_{\mu_1} \sum_{\mu_2} \sum_{m} F_{\mu_1} F_{\mu_2} \Lambda_m \left\{ \begin{array}{l} \cos\left[\left(\mu_{12} \pm mz\right)\theta - \tfrac{\mu_{12}}{p}\omega_0 t - 2\varphi_2\right] \\ +\cos\left[\left(\mu_{21} \pm mz\right)\theta - \tfrac{\mu_{21}}{p}\omega_0 t\right] \end{array} \right\} + \tfrac{\Lambda_0^2}{2\mu_0} \sum_{\mu} \sum_{h} F_\mu F_h \left\{ \begin{array}{l} \cos\left[\left(\mu + \nu\right)\theta - \left(\tfrac{\mu}{p} + h\right)\omega_0 t - \varphi_{23}\right] \\ +\cos\left[\left(\mu - \nu\right)\theta - \left(\tfrac{\mu}{p} - h\right)\omega_0 t - \varphi_{32}\right] \end{array} \right\} \\
& + \tfrac{\Lambda_0}{4\mu_0} \sum_{\nu} \sum_{\mu} \sum_{m} F_\nu F_\mu \Lambda_m \left\{ \begin{array}{l} \cos\left[\begin{array}{l}\left(\nu + \mu \pm mz\right)\theta \\ -\left(1 + \tfrac{\mu}{p}\right)\omega_0 t - \varphi_{12}\end{array}\right] \\ +\cos\left[\begin{array}{l}\left(\nu - \mu \pm mz\right)\theta \\ -\left(1 - \tfrac{\mu}{p}\right)\omega_0 t - \varphi_{21}\end{array}\right] \end{array} \right\} + \tfrac{\Lambda_0}{4\mu_0} \sum_{h} \sum_{\mu} \sum_{m} F_h F_\mu \Lambda_m \left\{ \begin{array}{l} \cos\left[\begin{array}{l}\left(\nu + \mu \pm mz\right)\theta \\ -\left(h + \tfrac{\mu}{p}\right)\omega_0 t - \varphi_{32}\end{array}\right] \\ +\cos\left[\begin{array}{l}\left(\nu - \mu \pm mz\right)\theta \\ -\left(h - \tfrac{\mu}{p}\right)\omega_0 t - \varphi_{23}\end{array}\right] \end{array} \right\} \\
& + \tfrac{F_0}{8\mu_0} \sum_{\mu} \sum_{m_1} \sum_{m_2} F_\mu \Lambda_{m_1} \Lambda_{m_2} \left\{ \begin{array}{l} \cos\left[\begin{array}{l}\left(p + \mu \pm \left(m_1 \pm m_2\right)z\right)\theta \\ -\left(1 + \tfrac{\mu}{p}\right)\omega_0 t - \varphi_{02}\end{array}\right] \\ +\cos\left[\begin{array}{l}\left(p - \mu \pm \left(m_1 \pm m_2\right)z\right)\theta \\ -\left(1 - \tfrac{\mu}{p}\right)\omega_0 t - \varphi_{20}\end{array}\right] \end{array} \right\}
\end{aligned}
\tag{24}
$$

REFERENCES

[1] G. Feng, C. Lai, K. L. V. Iyer, and N. C. Kar, "Improved high-frequency voltage injection based permanent magnet temperature estimation for PMSM condition monitoring for EV applications," *IEEE Trans. Veh. Technol.*, vol. 67, no. 1, pp. 216–225, Jan. 2018.

[2] C. Gong, Y. Hu, G. Chen, H. Wen, Z. Wang, and K. Ni, "A DC-bus capacitor discharge strategy for PMSM drive system with large inertia and small system safe current in EVs," *IEEE Trans. Ind. Informat.*, vol. 15, no. 8, pp. 4709–4718, Aug. 2019.

[3] C. Liu, G. Luo, X. Duan, Z. Chen, Z. Zhang, and C. Qiu, "Adaptive LADRC-based disturbance rejection method for electromechanical servo system," *IEEE Trans. Ind. Appl.*, vol. 56, no. 1, pp. 876–889, Jan./Feb. 2020.

[4] K. D. Hoang and H. K. A. Aorith, "Online control of IPMSM drives for traction applications considering machine parameter and inverter nonlinearities," *IEEE Trans. Transp. Electrific.*, vol. 1, no. 4, pp. 312–325, Dec. 2015.

[5] S. Morimoto, M. Sanda, and Y. Y. Takeda, "Wide-speed operation of interior permanent magnet synchronous motors with high-performance current regulator," *IEEE Trans. Ind. Appl.*, vol. 30, no. 4, pp. 920–926, Jul./Aug. 1994.

[6] J. Lu, Y. Hu, G. Chen, Z. Wang, and J. Liu. "Mutual calibration of multiple current sensors with accuracy uncertainties in IPMSM drives for electric vehicles," *IEEE Trans. Ind. Electron.*, vol. 67, no. 1, pp. 69–79, Feb. 2020.

[7] D. D. Reigosa, D. Fernandez, T. Tanimoto, T. Kato, and F. Briz, "Permanent-magnet temperature distribution estimation in permanent-magnet synchronous machines using back electromotive force harmonics," *IEEE Trans. Ind. Appl.*, vol. 52, no. 4, pp. 3093–3103, Jul./Aug. 2016.

[8] A. Cassat *et al.*, "A practical solution to mitigate vibrations in industrial PM motors having concentric windings," *IEEE Trans. Ind. Appl.*, vol. 48, no. 5, pp. 1526–1538, Sep/Oct. 2012.

[9] A. K. Putri, S. Rick, D. Franck, and K. Hameyer, "Application of sinusoidal field pole in a permanent-magnet synchronous machine to improve the NVH behavior considering the MTPA and MTPV operation area," *IEEE Trans. Ind. Appl.*, vol. 52, no. 3, pp. 2280–2288, May/Jun. 2016.

[10] Z. Xia, S. Nalakath, R. Tarvirdilu-Asl, Y. Sun, J. Wiseman, and A. Emadi, "Online optimal tracking method for interior permanent magnet machines with improved MTPA and MTPV in whole speed and torque ranges," *IEEE Trans. Power Electron.*, vol. 35, no. 9, pp. 9755–9771, Sep. 2020.

[11] A. S. Babel, J. G. Cintron-Rivera, and E. G. Strangas, "A multiple lookup table torque controller for improved performance of IPM machines," in *Proc. Int. Elect. Mach. Drives Conf.*, May 2013, pp. 521–525.

[12] L. Yan, M. Dou, Z. Hua, H. Zhang, and J. Yang, "Optimal duty cycle-model predictive current control of high-altitude ventilator induction motor with extended minimum stator current operation," *IEEE Trans. Power Electron.*, vol. 33, no. 8, pp. 7240–7251, Oct. 2018.

[13] C.-T. Pan and S.-M. Sue, "A linear maximum torque per ampere control for IPMSM drives over full-speed range," *IEEE Trans. Energy Convers.*, vol. 20, no. 2, pp. 359–366, Jun. 2005.

[14] T. Sun, J. Wang, M. Koc, and X. Chen, "Self-learning MTPA control of interior permanent magnet synchronous machine drives based on virtual signal injection," *IEEE Trans. Ind. Appl.*, vol. 52, no. 4, pp. 3062–3070, Jul./Aug. 2016.

[15] J. Pang, W. Liu, N. Jiao, J. Wang, and P. Ma, "Calculation of cross-coupling inductance and electromagnetic torque in wound-rotor synchronous starter/generator," *IEEE Trans. Ind. Electron.*, vol. 66, no. 7, pp. 5115–5123, Jul. 2019.

[16] M. Valavi, A. Nysveen, R. Nilssen, R. D. Lorenz, and T. Rølvåg, "Influence of pole and slot combinations on magnetic forces and vibration in low-speed PM wind generators," *IEEE Trans. Magn.*, vol. 50, no. 5, pp. 1–11, May 2014.

[17] R. Islam, I. Husain, A. Fardoun, and K. McLaughlin, "Permanent-magnet synchronous motor magnet designs with skewing for torque ripple and cogging torque reduction," *IEEE Trans. Ind. Appl.*, vol. 45, no. 1, pp. 152–160, Jan./Feb. 2009.

[18] J. W. Jiang, B. Bilgin, A. Sathyan, H. Dadkhah, and A. Emadi, "Noise and vibration reduction for IPMSM by using rotor circumferential slits," in *Proc. IEEE Int. Elect. Mach. Drives Conf.*, 2017, pp. 1–8.

[19] S. Park, S. Kim, W. Kim, J. Cho, and S. T. Lim, "A numerical model for predicting vibration and acoustic noise of IPMSM," in *Proc. IEEE Veh. Power Propulsion Conf.*, 2012, pp. 1054–1058.

[20] R. Islam and I. Husain, "Analytical model for predicting noise and vibration in permanent-magnet synchronous motors," *IEEE Trans. Ind. Appl.*, vol. 46, no. 6, pp. 2346–2354, Nov./Dec. 2010.

[21] C. Ma, Q. Liu, D. Wang, Q. Li, and L. Wang, "A novel black and white box method for diagnosis and reduction of abnormal noise of hub permanent-magnet synchronous motors for electric vehicles," *IEEE Trans. Ind. Electron.*, vol. 63, no. 2, pp. 1153–1167, Feb. 2016.

[22] D. Torregrossa, A. Khoobroo, and B. Fahimi, "Prediction of acoustic noise and torque pulsation in PM synchronous machines with static eccentricity and partial demagnetization using field reconstruction method," *IEEE Trans. Ind. Electron.*, vol. 59, no. 2, pp. 934–944, Feb. 2012.

[23] P. Pellerey, V. Lanfranchi, and G. Friedrich, "Coupled numerical simulation between electromagnetic and structural models. Influence of the supply harmonics for synchronous machine vibrations," *IEEE Trans. Magn.*, vol. 48, no. 2, pp. 983–986, Feb. 2012.

[24] I. P. Tsoumas and H. Tischmacher, "Influence of the inverter's modulation technique on the audible noise of electric motors," *IEEE Trans. Ind. Appl.*, vol. 50, no. 1, pp. 269–278, Jan./Feb. 2014.

[25] F. Lin, S. Zuo, W. Deng, and S. Wu, "Modeling and analysis of electromagnetic force, vibration, and noise in permanent-magnet synchronous motor considering current harmonics," *IEEE Trans. Ind. Electron.*, vol. 63, no. 12, pp. 7455–7466, Dec. 2016.

[26] J. Jung, S. Lee, G. Lee, J. Hong, D. Lee, and K. Kim, "Reduction design of vibration and noise in IPMSM type integrated starter and generator for HEV," *IEEE Trans. Magn.*, vol. 46, no. 6, pp. 2454–2457, Jun. 2010.

[27] D. Torregrossa, D. Paire, F. Peyraut, B. Fahimi, and A. Miraoui, "Active mitigation of electromagnetic vibration radiated by PMSM in fractional-horsepower drives by optimal choice of the carrier frequency," *IEEE Trans. Ind. Electron.*, vol. 59, no. 3, pp. 1346–1354, Mar. 2012.

[28] M. S. Islam, R. Islam, and T. Sebastian, "Noise and vibration characteristics of permanent-magnet synchronous motors using electromagnetic and structural analyses," *IEEE Trans. Ind. Appl.*, vol. 50, no. 5, pp. 3214–3222, Sep./Oct. 2014.

[29] F. Ishibashi, K. Kamimoto, S. Noda, and K. Itomi, "Natural frequency of stator core of small induction motor," *Proc. Inst. Elect. Eng.—Elect. Power Appl.*, vol. 150, no. 2, pp. 210–214, Mar. 2003.

Zexiu Han (Member, IEEE) was born in Shaanxi, China, on May 4, 1990. He received the B.Eng. and M.Eng. degrees in electrical engineering in 2013 and 2015, respectively, from Northwestern Polytechnical University, Xi'an, China, where he is currently working toward the Ph.D. degree with the School of Automation.

His research interests include electrical machines design and drives, power electronics, and motion control.

Jinglin Liu (Member, IEEE) received the B.Eng. degree from Tsinghua University, Beijing, China, in 1986, and the M.Eng. and Ph.D. degrees from the Northwestern Polytechnical University (NWPU), Xi'an, China, in 1990 and 2002, respectively, all in electrical engineering.

Since 1994, he has been a Faculty Member with NWPU, where he is currently a Professor of Electrical Engineering. His research interests include electrical machines design and drives, power electronics, fault diagnosis, and motion control.